

¹ Wind Veer and Speed in Turbulent Ekman Flow - Part 1:
² Scaling analysis and universal profile model

³ Cedrick Ansorge¹ and Hauke Wurps²

⁴
⁵ Submitted October 17, 2024

⁶ **Abstract**

⁷ The profiles of wind speed and direction in turbulent Ekman flow are formulated
⁸ based on asymptotic theory and data from direct numerical simulation. The profile
⁹ of the streamwise component follows the classical viscous, logarithmic and wake
¹⁰ scaling. In the outer layer, the velocity component profiles can be described by an
¹¹ Ekman-spiral with adapted boundary conditions that result in a reduction of the
¹² spiral-like rotation. The span-wise component poses a conceptual challenge to the
¹³ channel-flow analogy in the context of asymptotic matching; it exhibits a mixed
¹⁴ scaling in the surface layer, but follows outer scaling for most of the outer layer.
¹⁵ Viscous stress scales universally across the boundary layer in inner units while
¹⁶ the total stress becomes universal as a function of outer height. This implies a
¹⁷ mixed scaling for the turbulent stress and eddy viscosity across the inner layer
¹⁸ and convergence to a universal scaling as function of the outer height across the
¹⁹ outer layer for increasing scale separation vide Reynolds numbers.

²⁰ **1 Introduction**

²¹ The Coriolis force bends the path of motion on a rotating sphere and establishes
²² geostrophic equilibrium when in balance with a pressure gradient force. Wind veer
²³ away from the wind direction in geostrophic equilibrium is (i) due to direct fric-
²⁴ tional effects in the very vicinity of the surface and (ii) due to turbulence which
²⁵ exerts indirect frictional effects; these effects cause a slow-down of the mean wind
²⁶ reducing the Coriolis force thus turning the wind in favor of the pressure gradient
²⁷ force. Not only does the veering set the frame of reference for surface layer theory,
²⁸ it also has effects at small and large scales from large-scale dispersion via plume
²⁹ spreading to cyclone spin-down (Svensson and Holtslag 2009) and on the capa-
³⁰ bilities of data assimilation and accuracy of surface flux estimates (Brown et al.
³¹ 2005). From a large-scale perspective, the veering of wind across the planetary

¹ FU Berlin, Institut für Meteorologie, Carl-Heinrich-Becker-Weg 6–10, 12165 Berlin
cedrick@posteo.de

² Uni Oldenburg

boundary layer determines the amount of cross-isobaric mass-flux, commonly referred to as 'Ekman pumping' (Ekman 1905), and it is thus a key factor in the life-cycle of large-scale synoptic systems. Within the atmospheric boundary layer (ABL), directional shear of the wind in the upper part of the surface layer may cause a systematic yaw for tall wind power generation devices where blades reach into the Ekman layer, i.e. that part of the boundary layer where the wind starts to turn; an exact estimate of such effects is critical in the site assessments for wind farms (Calaf et al. 2010; Mirocha et al. 2018).

In the planetary boundary layer, wind veer is characterized by the surface veering angle α defined as the angle between the negative surface shear stress τ_{sfc} and the geostrophic wind. Surface veering α and geostrophic drag $Z \equiv u_*/G$, where the friction velocity $u_* \equiv \sqrt{|\tau_{\text{sfc}}|/\rho}$, uniquely determine the surface drag τ_{sfc} in a turbulent Ekman flow. In any quantitative description of the surface layer, the friction velocity u_* is the dynamic scale and α defines the alignment of the frame of reference. Knowledge about u_* and α is thus a prerequisite for any quantitative theory of the surface layer, and Rossby and Montgomery (1935) constrained the two parameters based on integral relations in the ABL. Asymptotic similarity theory was later used by Tennekes (1973); Blackadar and Tennekes (1968), and—based on his seminal direct numerical simulations (DNS) of Ekman flow—Spalart (1989) suggested a modification to take into account effects of low to intermediate Reynolds numbers. Later on, constants were re-evaluated with a focus on the ABL based on observations (Högström 1988, 1996) and numerical modelling (Spalart et al. 2008, 2009; Ansorge and Mellado 2014; Ansorge 2019).

Attempts were also undertaken to obtain profiles of the wind speed: One approach is to match the inner and outer layer at a reference height; Etling (2002); Emeis (2018) (Sec. 21.10; Eq. 21.48) choose the Prandtl-layer height z_{Prandtl} to match the wind speed profiles, which, however, requires external prescription of $\alpha(z_{\text{Prandtl}})$, the veering at that height. A one-dimensional profile with constant veering is given by Emeis et al. (2007, Sec. 3; Eq. 3.1-3.19).

Gryning et al. (2007) present an extension of the wind-speed profile beyond the surface layer using a neutral reference profile and a stability correction; Kelly and Gryning (2010), based on a probabilistic representation of stratification, develop a model for the long-term mean wind speed in the ABL and compare this with observation at different sites; Kelly and Troen (2016) demonstrate the effect of such improved model for wind-energy applications. In consideration of the large scale separation in geophysical flow, the rotation of the wind in the surface layer is often assumed negligible, and above investigations merely focus on the wind speed; that means, the veering of the wind with height is not described and there is little knowledge on the profile of the span-wise velocity component and the precise shape of the hodograph in the limit of a truly neutral Ekman boundary layer. A climatology of wind turning in the ABL is given by Lindvall and Svensson (2019) Klein et al. (2021) use a statistical turbulence modelling approach that yields a two-component velocity profile, but they also find that the exact representation of turning is challenging.

Ekman-layer models are roughly based on Ekman's seminal 1905 paper in combinations with additional assumptions, such as a prescribed profile shape for eddy viscosity Ellison (1955) and two-layer models of the ABL take into account rotational effects at higher altitudes, for instance when the wind speed needs to be evaluated at heights on the order of 100 – 200 m, a particular concern when

it comes to wind-power forecasting (Optis et al. 2014). Despite rotational effects being considered, the formulation of these models for the outer layer and analysis of their performance primarily focuses on wind speed. Still, in 2018, Jiang et al. recognized that the outer part of the Ekman boundary layer receives less attention in comparison with the surface layer and study the neutral problem by Large-Eddy simulation (LES). They focus on the wind speed and find an extended logarithmic layer when considering the wind speed instead of the shear-aligned component, and they eventually demonstrate by means of an analytical model that this vertical extension of the logarithmic layer may be explained by a transfer of stress to the span-wise velocity component where it is assumed that the shear vector $\tau(z)$ and stress vectors $(\partial_z U, \partial_z V)$ are aligned.

More recently, Ghannam and Bou-Zeid (2021) treated the horizontally averaged momentum budget to show that departures from shear-alignment in the vicinity of the surface result in an integral of the wind veer (α_M in their notation) over the height to very high accuracy ($\int_{z_0}^H \sin \alpha_M$ in their notation; their Eq. (16)). Classic surface-layer similarity is recovered when the angle α_M does not depend on height, i.e., the wind veer is constant across the surface layer. If, however, the wind veer depends on height, the profiles of stress and mean velocities depart from the scalings implied by classic surface-layer similarity.

Turbulent Ekman flow is considered here as a conceptual model of the homogeneous, stationary ABL over a flat surface under neutral stratification. Universal profiles of the wind vector for turbulent Ekman flow not only are a well-described limit for theoretical exploration or higher-order approaches taking into account possible effects of stratification, roughness or other physical complications encountered in the real geophysical system. While, on first sight, the study of such a strongly idealized case appears as an academic problem, it contains the essence of surface similarity as it is used in most atmospheric models, be it conceptual or numeric ones. More complex accounts generally refer to the homogeneous stationary problem as a base state: (i) Roughness is commonly incorporated by a linear transformation of vertical scale involving the roughness parameter z_0 and for larger roughness also a displacement height (Monin and Yaglom 1975; Jacobs and Van Boxel 1988; Högström 1988); (ii) Stability can be accounted for by a linearization around the neutrally stratified profile (Monin 1970; Monin and Yaglom 1975; Högström 1988, 1996; Sakagami et al. 2020); (iii) Non-stationarity in the pressure-gradient forcing can be accounted for by a linear damped-oscillator approach around the base state (Momen and Bou-Zeid 2016); (iv) Barotropic and baroclinic effects on the velocity profile require to consider the height-dependence of the veer and stress misalignment (Momen et al. 2018; Ghannam and Bou-Zeid 2021). Furthermore, such a solution can serve as better initial condition for numerical simulation of the flow, to minimize the length of initial transient periods, or as benchmark for turbulence closures that can be tuned to reproduce the neutral limit case.

Despite the strong simplifications implied by our choice of set-up, there is no straightforward approach to solving this well-defined problem. Large-Eddy simulation not only needs to be tuned for the surface shear stress and veering angle, but it also relies on sub-grid closures that commonly assume alignment of the turbulent stress with gradients. This pre-requisite is not fulfilled when the wind rotates with height. Esau (2004) investigated the representation of the Ekman boundary

layer by dynamical subgrid closures and Zikanov et al. (2003) proposed a closure for the wind profile using a linearized representation of the eddy viscosity. Despite advances in analysis of this simplified set-up (Jiang et al. 2018), there is yet insufficient understanding for a quantitative generalization of the results to arbitrary external forcing (manifest in variation of the Reynolds number) – and indeed the fundamental questions pertaining to such relatively simple dynamics of turbulence are not reflected in the research on LES for the ABL over the past 50 years (Stoll et al. 2020).

At the same time, an increasing amount of high-quality and high-resolution data from turbulence-resolving approaches is emerging due to recent advances in high-performance computing and its application to geophysical problem sets; the geophysical range of scale separation, however, is—and it will remain so for the foreseeable future—out of reach for such simulation (Dimotakis 2005). Here, the routinely employed concept of Reynolds-number similarity can help. It postulates the existence of *fully developed turbulence* believed to occur for a sufficiently large but finite Reynolds number (Barenblatt and Goldenfeld 1995). (Already in 1998, this ~~in fact lead~~ Moin and Mahesh to the question *how high a Re is high enough?*) Certain statistics of fully developed turbulence, such as dissipation (Dimotakis 2005) or profiles of mean velocity (Barenblatt 1993), become independent of the Reynolds number when appropriately scaled; other statistics, such as the near-wall maximum in velocity fluctuation depend on Re (Baars and Marusic 2020) and externality of the flow may exert an impact on near-wall scaling (da Silva et al. 2014). It appears that for certain statistics in Ekman flow, fully-developed turbulence is reached with the Reynolds numbers that became possible due to an increase of computing capabilities over the past decades.

This paper exploits the robust features of mean velocity profiles from direct numerical simulation across a range of Reynolds numbers to formulate both the streamwise and span-wise components of the mean velocity vector as a function of the Reynolds number.

2 Problem Formulation and Numerical Approach

We consider here incompressible, turbulent Ekman flow, that is, the turbulent flow over a flat rotating plate, as a physical model for the truly neutral ABL. The f-plane approximation is applied such that rotation only acts on horizontal velocity components; we thus neglect rotational effects on the horizontal components of velocity and dynamical effects due to latitudinal variation of the rate of rotation.

2.1 Notation and Governing Equations

The dimensional velocity vector of the numerical simulations is $\underline{U} = (U_1, U_2, U_3) = (U, V, W)$ over the coordinate system $Oxyz$, where an approximate alignment (plus/minus few degrees) of the direction Ox with the surface shear stress is achieved. The coordinate Oz points away from the wall, and Oy points in the span-wise direction normal to Oxz . For analysis of the results, we use two coordinate systems that are



170 (i) exactly aligned with the surface shear stress

$$\underline{\tau}_{\text{sfc}} = \begin{pmatrix} \tau_x \\ \tau_y \\ \tau_z \end{pmatrix} = -\nu \left(\frac{\partial U}{\partial z} \hat{e}_x + \frac{\partial V}{\partial z} \hat{e}_y \right) \quad (1a)$$

171 and labelled by an upper index α as in \underline{U}^α for the velocity vector, and (ii) the
 172 coordinate system aligned with the free-atmosphere geostrophic wind labelled by
 173 an upper index G as in \underline{U}^G . We denote the modulus of the surface shear, the
 174 surface friction, by

$$u_* = \sqrt{\|\underline{\tau}_{\text{sfc}}\|} \quad (1b)$$

175 and let $Z_* = G/u_*$; the surface veering angle α_* is the angle between $\underline{\tau}$ and the
 176 geostrophic wind

$$\alpha_* = \sphericalangle(\underline{G}, \underline{\tau}_{\text{sfc}}). \quad (1c)$$

177 Analogously, we denote the height-local veering of the wind $\alpha(z) = \sphericalangle(\underline{G}, \underline{U}(z))$,
 178 where $\underline{G} = (G_1, G_2, 0)$ is the geostrophic wind vector.

179 We consider the incompressible Navier–Stokes equations for the three velocity
 180 components on the f-plane in a framework that is governed by (i) geostrophic wind
 181 magnitude $G = \sqrt{G_1^2 + G_2^2}$, (ii) Coriolis parameter f (representing the angular
 182 rotation), and (iii) kinematic viscosity ν . In absence of external variability, this
 183 system converges to a statistically steady state in the sense that flow statistics
 184 do not depend on time; and this state is defined by a Reynolds number, the only
 185 non-dimensional parameter that governs the system. We use the geostrophic wind
 186 as velocity and the Coriolis parameter f as time scale for the non-dimensional
 187 framework. This implies the Rossby radius $A_{\text{Ro}} = G/f$ as length scale, such that
 188 one Reynolds number governing the problem reads as

$$\text{Re}_A = \frac{GA_{\text{Ro}}}{\nu}. \quad (2)$$

189 The scales used in defining Re_A are of limited relevance for description of the
 190 turbulent flow state. The turbulence scale separation in a wall-bounded flow is
 191 commonly characterized by the friction Reynolds number (Jiménez 2012):

$$\text{Re}_\tau = \frac{u_* \delta}{\nu} = \delta^+ = \frac{\text{Re}_A}{Z_*^2}, \quad (3)$$

192 where $\delta = u_*/f$ and we use a superscript '+' to denote normalization by inner
 193 turbulence scales (u_*, ν) . Another common measure of scale separation is the
 194 Reynolds number defined by the laminar Ekman layer thickness $D = \sqrt{2\nu/f}$,

$$\text{Re}_D = \frac{GD}{\nu} = \sqrt{2\text{Re}_A}. \quad (4)$$

195 ~~Another common measure of scale separation is the Reynolds number defined by~~
 196 ~~the laminar Ekman layer thickness $D = \sqrt{2\nu/f}$~~ ,

$$\text{Re}_D = \frac{GD}{\nu} = \sqrt{2\text{Re}_A}. \quad (5)$$

197 The governing equations non-dimensionalized by G , f , and Λ_{Ro} read as

$$\frac{\partial u_i}{\partial t} = \frac{\partial \pi}{\partial x_i} - u_j \frac{\partial u_i}{\partial x_j} + \epsilon_{i2j}(u_j - G_j) + \frac{1}{\text{Re}} \frac{\partial^2 u_i}{\partial x_j^2} \quad (6a)$$

$$\frac{\partial u_j}{\partial x_j} = 0, \quad (6b)$$

198 where $u_i = U_i/G$ are the non-dimensional components velocity, π is non-dimen-
 199 sional pressure, $g_j = G_j/G$ are non-dimensionalized components geostrophic wind
 200 (with $g_1^2 + g_2^2 = 1$ by construction), and ϵ is the Levi–Civita tensor. These equations
 201 are solved inside a bounded cube of size $L_x \times L_y \times L_z$ with periodic boundary condi-
 202 tions in the lateral (streamwise and spanwise) directions, a no-slip–no-penetration
 203 boundary at $z = 0$, and a no-penetration, free-slip boundary at $z = L_z$.

204 **2.2 Numerical Simulations**

205 The problem is solved numerically by tLab¹, an open-source tool-suite to simulate
 206 and analyze turbulent flows. We use here a fourth-order–five-step Runge–Kutta
 207 integration and sixth-order compact schemes for spatial derivatives in all direc-
 208 tions. The incompressibility constraint is enforced by a fractional step approach
 209 where the Poisson equation for the pressure field is solved to machine accuracy
 210 using a combined spectral/compact approach as described in Mellado and Ansorge
 211 (2012).

212 Simulations used here are shown in Tab. 1. We extend an existing set of simula-
 213 tions for $\text{Re}_A \in \{125\,000; 281\,250; 500\,000\}$ (gray shading; cf. Ansorge and Mellado
 214 2014, 2016) by new simulations at higher Reynolds numbers up to $\text{Re}_A = 1.28 \times 10^6$
 215 with a horizontal domain extent up to 3.3×10^4 viscous units. In total, this yields
 216 one order of magnitude variation in terms of the scale separation in the boundary
 217 layer.

218 **3 Scaling behavior of the flow for Re_τ up to 3000**

219 The generalization of profiles to arbitrary Reynolds numbers requires sufficient
 220 scale separation in the simulations, not only to quantify the effect of the Reynolds
 221 number on low-order flow statistics, but also to assess the corresponding rate-of-
 222 change to eventually allow for an extrapolation of the findings. While the simula-
 223 tions previously available (gray shading in Tab. 1) give confidence in a first-order
 224 representation of the turbulent problem, the estimation of higher-order effects such
 225 as the dependency of the Reynolds number requires a broader scale separation that
 226 is made available by the two new simulations at increased Reynolds number (cf.
 227 Tab. 1). Data at such scale separation has been obtained previously (cf. Spalart
 228 et al. 2008, 2009), but we also need high confidence with respect to the convergence
 229 of simulation data for slow oscillations and with respect to sampling convergence,
 230 which translates to two further requirements on the data: First, data should be free

¹ <https://github.com/turbulencia/tlab>

Table 1 Direct numerical simulation data sets used in this work. Re_A and Re_D refer to the Reynolds number defined in terms of the Rossby radius Λ and Ekman-layer thickness D respectively. L_{xy} is the domain size in the stream- and span-wise direction. The grid is given by the number of grid points in the stream-wise (N_x), span-wise (N_y) and vertical (N_z) directions respectively. The resolution in the span-wise and stream-wise directions are given as Δx^+ and Δy^+ . The grid in the vertical is stretched, and resolution at the wall is given by $\Delta z^+|_{z=0}$.

Re_A	Re_D	L_{xy}/Λ	$N_x \times N_y \times N_z$	Δx^+	Δy^+	$\Delta z^+ _{z=0}$
125 000	500	1.08	$2048 \times 2048 \times 192$	4.1	4.1	1.05
281 250	750	1.08	$3072 \times 3072 \times 384$	5.6	5.6	1.60
500 000	1 000	1.08	$3072 \times 6144 \times 512$	9.3	4.7	1.14
845 000	1 300	0.54	$2560 \times 5120 \times 640$	8.9	4.5	0.99
1 280 000	1 600	0.54	$3860 \times 7680 \times 960$	8.6	4.3	1.00

Table 2 DOIs and reference to the openly accessible data set at refubium repository

Re_D	DOI	Reference
500	10.17169/refubium-42505	Ansorge (2024a)
1000	10.17169/refubium-42507	Ansorge (2024b)
1300	10.17169/refubium-42508	Ansorge (2024c)
1600	10.17169/refubium-42509	Ansorge (2024d)

of artifacts from long-term oscillations across the vertical extent of the domain—primarily, simulations should be free of effects originating from the inertial oscillation; this is achieved here by replacing the mean value of the three-dimensional velocity fields by the time mean over a whole inertial oscillation. Second, high accuracy is also needed in terms of the statistical convergence of averages, bulk measures and large-scale structures; this requires a domain size $L_x > \mathcal{O}(\delta_{95})$. We use here $L_x = L_y = 1.08\Lambda$ for cases with $Re \leq 1000$ and $L_x = L_y = 0.54\Lambda$ for $Re \geq 1300$ which corresponds to $L_x/\delta_{95} \approx 25$ for $Re_D = 500$ and $L_x/\delta_{95} \approx 18$ for $Re_D = 1300$.

Bulk parameters of the simulations are given in Tab. 3. The surface stress is characterized by u_* and α_* in relation to the geostrophic wind vector and discussed in more detail as the drag law below in Sec. 4.1 (we find the expected slight decrease of u_* and α_* with increasing Re). The boundary-layer height estimated from the 95% stress reduction, δ_{95} , is around 0.6δ to 0.66δ . Interestingly, the integrated TKE $\int_0^\delta edz$ stays constant when normalized by the friction velocity u_* while the integrated dissipation $\int_0^\delta edz$ exhibits inviscid scaling when normalized by the magnitude G of the geostrophic wind. (TKE and dissipation normalized as $fG^{-3} \int edz$ and $u_*^{-3} \int edz$, exhibit substantial dependence on Re for the variation of u_* .) This indicates that the bulk dissipation is governed by the forcing G -irrespective of Re . Changes in Re , however, affect the level and organization of turbulence, and the parameter representing this dependency is the friction velocity u_* which describes the turbulence production processes in the surface layer, in particular in the buffer layer.

Velocity profiles in inner units ($U^+(z^+)$, Fig. 1a) and outer units ($U^-(z^-)$, Fig. 1b) are in accordance with previous work (Coleman et al. 1992; Spalart et al. 2008, 2009; Ansorge and Mellado 2014; Ansorge 2019): The profiles of the shear-aligned streamwise velocity component are well-collapsed for $Re_D > 500$ below $z^- \approx 0.15$ (circles in Fig. 1a); the case with $Re_D = 500$ is only transitionally

Table 3 Bulk characterization of the simulations for different Reynolds numbers. Viscous Reynolds number Re , friction Reynolds number Re_τ , friction velocity u_* , surface veering angle α_* , normalized boundary layer depth δ_{95}/δ , inner normalization of vertically integrated TKE, outer normalization of vertically integrated dissipation.

Re	$\delta^+ = \text{Re}_\tau$	u_*	α_*	δ_{95}/δ	$f u_*^{-3} \int_0^\delta \epsilon dz$	$G^{-3} \int_0^\delta \epsilon dz$
500	479	0.0619	25.5	0.66	0.88	1.31
750	886	0.0561	21.0	0.65	0.90	1.34
1000	1403	0.0530	18.8	0.62	0.92	1.30
1300	2122	0.0501	17.9	0.59	0.85	1.24
1600	2978	0.0482	17.2	0.61	0.91	1.21

turbulent and there is no distinct inner-outer scale separation. The logarithmic law is appropriate for $50 < z^+ < 0.15 \text{Re}_\tau$, where $z^+ = \text{Re}_\tau z^-$. While the profiles $U^{\alpha*+}(z^+)$ diverge between different Re beyond $z^- = 0.15$, the corresponding profiles of the velocity deficit $(U^{\alpha*}(z^-) - G_1^\alpha)/u_*$ agree closely, irrespective of Re . This illustrates the inner–outer scale-duality in this external flow with inner scaling being appropriate in the inner layer and outer scaling in the outer layer. Also in the outer layer of the flow, u_* (and not the magnitude of the geostrophic wind G) governs the inviscid normalization, i.e. a scaling independent of the Reynolds-number.

No collapse is found for the profiles of spanwise velocity when considered in inner units, $V^{\alpha*+}(z^+)$. When normalized in outer units, the deficit profiles of spanwise velocity $(V^{\alpha*}(z^-) - G_2^\alpha)/u_*$ agree well beyond $z^- \approx 0.3$. This is a much higher level in comparison with the streamwise component that collapses also within the overlap layer, i.e. much closer to the surface (circles in Fig. 1b). The value of $V^{\alpha*+}(z^-) - G_2^\alpha$ is sensitive to the wind veering for $z \rightarrow 0$ as—for use of the shear-aligned component—it has to approach the value $-G_2^\alpha = |G| \sin \alpha \neq 0$ in view of the no-slip boundary condition. While low-Re effects appear to be present for $\mathcal{O}(\text{Re}) < 10^3$, the spanwise component converges to an Re -independent limit within the range of scale separation considered here, i.e.

$$G_2^\alpha/u_* = Z_* \sin \alpha \rightarrow \text{const. for } \text{Re} \rightarrow \infty, \quad (7)$$

which has indeed already been found by Spalart (1989), who estimates the constant from an integral relation.

The viscous stress

$$S_{\text{visc}} = \nu \sqrt{\left(\frac{\partial U}{\partial z} \right)^2 + \left(\frac{\partial V}{\partial z} \right)^2} \quad (8a)$$

exhibits universal scaling when considered as $S_{\text{visc}}^+(z^+)$ (Fig. 2a); this normalization is also appropriate in the outer layer where the viscous stress is, however, small. Small deviations from the universal profile are observed for the smallest Reynolds number $\text{Re} = 500$; we attribute these to low-Re effects in the only transitionally turbulent flow ($\text{Re}_\tau = 479$). In contrast to the viscous stress, the total stress follows outer normalization, i.e. $S^+(z^-)$ is universal; a discrepancy in the inner layer does not occur as the total stress is approximately constant in the viscous and buffer layer, and a rescaling of the height would have no effect there;

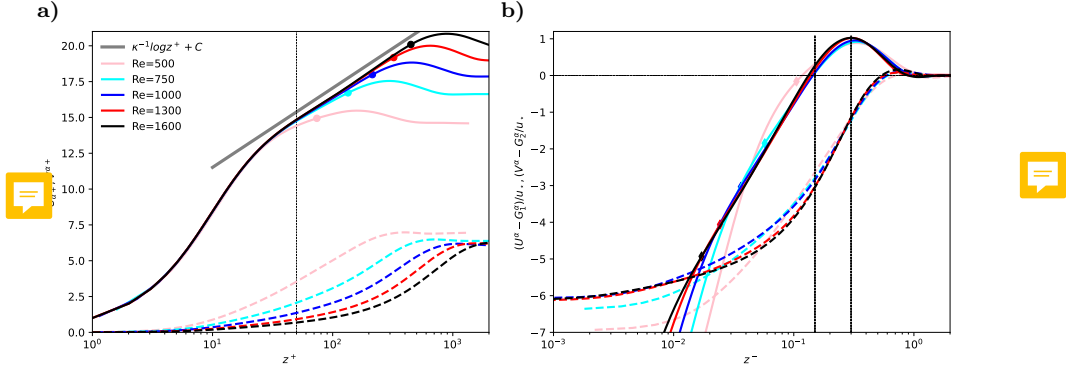


Fig. 1 a) Shear-aligned velocity profiles in inner units; b) Shear-aligned velocity deficit in outer units; circles mark the height $z^- = 0.15$; dashed line gives the best logarithmic fit to the data.

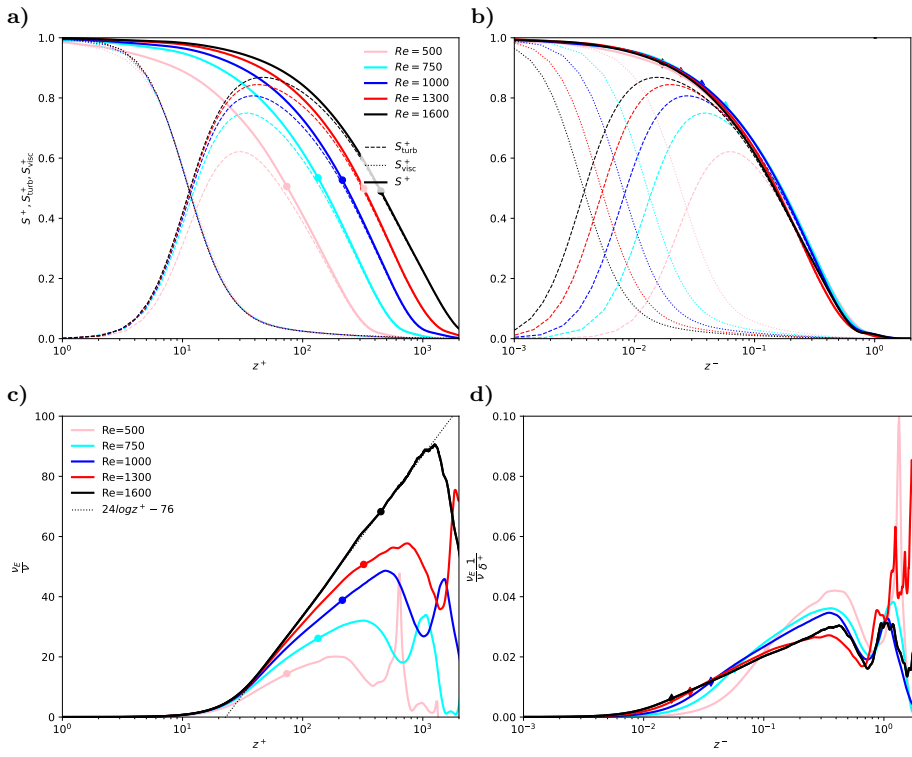


Fig. 2 a-b) Profiles of the turbulent stress S_{turb}^+ (dashed), the viscous stress S_{visc}^+ (dotted), and the total stress, $S^+ = S_{\text{visc}}^+ + S_{\text{turb}}^+$ (solid) as a function of inner height (a) and outer height (b). c-d) Normalized eddy viscosity ν_E (solid) plotted versus inner (c) and outer height (d). Different colors are for different Reynolds numbers (cf. Tab. 1). Circles in (a) and (c) denote the height $z^- = 0.15$, diamonds in (b) and (d) are for $z^+ = 50$ as in Fig. 1.

above, outer scaling is appropriate for the well-established dynamics in the overlap region of inner and outer layer. This, however, implies a mixed scaling for the turbulent stress,

$$S_{\text{turb}} = \sqrt{\overline{uw}^2 + \overline{vw}^2}. \quad (8b)$$

Indeed, S_{turb} only follows inner normalization below $z^+ \lesssim 20$ (where the turbulent contribution is negligible). In the outer layer, where $S_{\text{visc}} \rightarrow 0$, S_{turb}^+ follows outer normalization for $z^- \gtrsim 0.15$ —with increasing accuracy for larger Re and larger distance from the surface. In the overlap region, i.e. for $z^+ > 20$ and $z^- < 0.15$, the mixed scaling for the turbulent stress can be expressed as

$$S_{\text{turb}}^+(z^+, \text{Re}_\tau) = S^+(z^-) - S_{\text{visc}}^+(z^+), \quad (8c)$$

where $z^- = z^+/\text{Re}_\tau$.

The Eddy viscosity plays a crucial part when modelling profiles and the vertical transport in turbulent flow. In analogy to the Fick-law for molecular diffusion, the eddy diffusivity is the effective diffusivity that yields the turbulent transport S_{turb} based on the strain rate. For the symmetries in the flow (horizontal homogeneity, and $W = 0$), it is

$$\nu_E = \frac{S_{\text{turb}}}{\sqrt{\left(\frac{\partial U}{\partial z}\right)^2 + \left(\frac{\partial V}{\partial z}\right)^2}} = \nu \frac{S_{\text{turb}}}{S_{\text{visc}}}. \quad (9a)$$

The inner normalization of ν_E is obtained when dividing by the molecular viscosity:

$$\nu_E^+ = \nu_E/\nu = S_{\text{turb}}/S_{\text{visc}}. \quad (9b)$$

Under this normalization, the profiles of eddy viscosity collapse below $z^+ \approx 20$ with a tendency towards better collapse at higher z^+ for higher Reynolds number (up to $z^+ \approx 50$ for $\text{Re} = 1600$; Fig. 2c). In the outer layer, the eddy viscosity is characterized by a distinct minimum at $z^- \approx 0.6 - 0.8$, and we find that the following mixed normalization of ν_E by the geostrophic wind and friction velocity collapses the value of ν_E at this minimum (cf. Fig. 2d):

$$\nu_E^- = \nu_E^+ \frac{1}{\delta^+} = \nu_E \frac{1}{\nu} \frac{\nu}{u_* \delta} = \nu_E \frac{f}{u_*^2}. \quad (9c)$$

Substantial variation of the profiles is, however observed below and above this minimum for different Re which illustrates that this normalization is probably not generally appropriate across the outer layer.

The organization of the flow is depicted in terms of the turbulence kinetic energy in Fig. 3. In vicinity of the wall, at $y^+ \approx 10$, (Fig. 3a), elongated streaks aligned with the surface shear stress dominate. Moving away from the wall, to $y^+ \approx 150$ (well within the logarithmic region), the structures are larger and more isotropic, but they are still largely aligned with the surface shear stress. In the upper part of the outer layer, around $y^+ \approx 1000$, no clear signature of the surface veering direction is found, and intense TKE structures (bright yellow) are organized on a large spatial scale with weaker eddies (greenish structures) and quiescent regions in between.



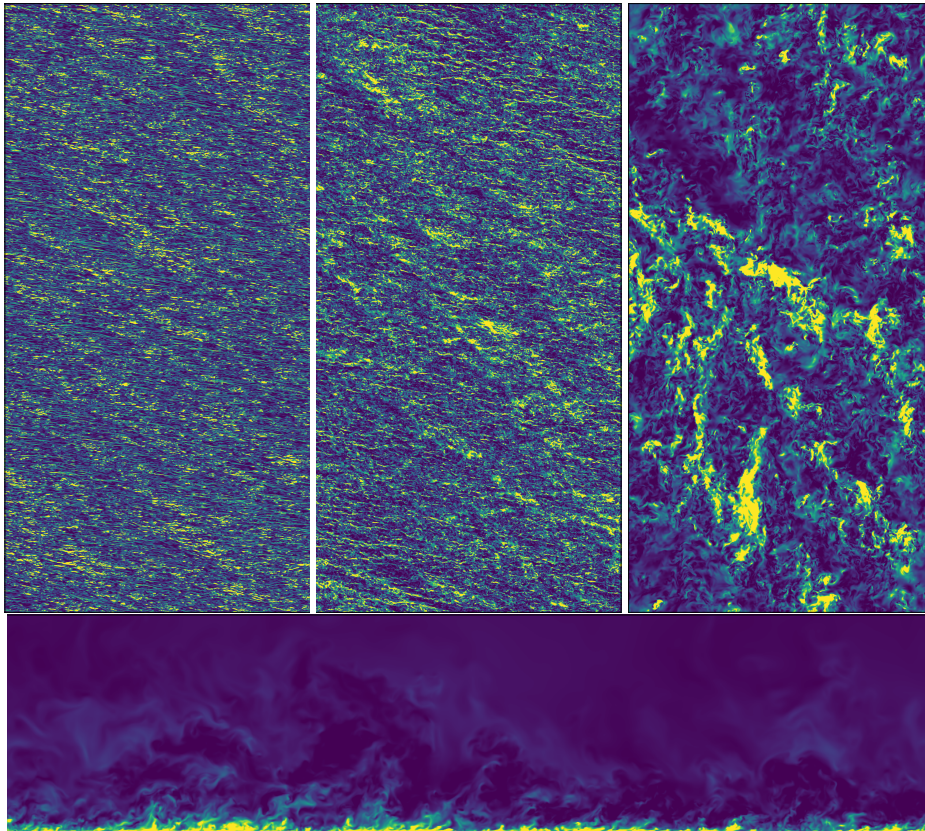


Fig. 3 horizontal slices of turbulence kinetic energy in the Buffer layer ($i=10$), logarithmic Layer ($i=100$), and outer layer ($i=400$); coloring between percentiles 4 and 96 of the respective image. Lower panel: streamwise–vertical intersect through the domain



322 4 A universal velocity profile for the turbulent Ekman layer

323 We now turn to the formulation of a general velocity profile that is fully determined
 324 by the only parameter of the idealized problem, namely a Reynolds number repre-
 325 senting the scale separation or geometric size of the problem. This precludes, first,
 326 a drag law wherewith we begin this section (4.1). Based on the scaling arguments
 327 put forward in Sec. 3, we then develop, second, a formulation of the wind vector
 328 in the Ekman layer (Sec 4.2). Finally, we come up with a separate formulation of
 329 the, third, stream-wise and, fourth, span-wise velocity components in the overlap
 330 and inner regions of the flow.

331 4.1 Drag-Law

332 A drag-law for Ekman flow determines—as a function of Reynolds number alone—
 333 the surface drag. This can be formulated by the normalized surface friction, u_*
 334 (Eq. (1b), also termed geostrophic drag), and the direction of surface shear stress,

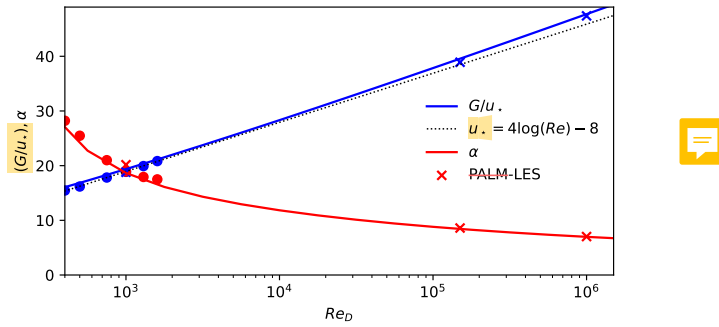


Fig. 4 Variation of geostrophic drag, Z_* , and surface veering, α_* , with Reynolds number according to the theory by Spalart et al. (1989) and as estimated from DNS data.

335 α_* (Eq. (1c), also termed wind veer). A non-zero veering of the wind is a rather
 336 special case in comparison with most turbulent flows considered in an engineering
 337 context, and it confronts us with a situation where the most appropriate coordinate
 338 system for analysis (namely that aligned with the surface shear stress) is a priori
 339 unknown. We compare our DNS data against a semi-empirical drag-law based on
 340 integral consideration (Spalart 1989) and find, as demonstrated in previous work
 341 (Ansorge and Mellado 2014), excellent agreement in the range $400 < \text{Re} < 1600$,
 342 representing a factor of 16 in variation of viscosity.

343 We also find that the solution of the transient equation involved in estima-
 344 tion of u_* for a given Reynolds number Re_D is approximated reasonably by the
 345 formulation

$$Z_* = 4 \log(\text{Re}_D) - 8 \quad (10)$$

346 which quantifies the 'weak' dependence of u_* on the Reynolds number as an ap-
 347 proximately logarithmic one, at least for problems with a scale separation on the
 348 order that is relevant to geophysical problems ($Re_D < 10^8$).

349 4.2 Profile in the Ekman layer

350 Formulations for the outer layer that take into account the rotation (and thus
 351 deviation from the channel-flow analogy) need to be matched to the framework of
 352 surface similarity. A smooth transition from the inner layer to the Ekman layer,
 353 where the wind is characterized by a turning of its mean direction, is not eas-
 354 ily achieved. Optis et al. (2014), for instance, define an "effective geostrophic wind
 355 vector that has the same magnitude of the observed surface geostrophic wind and is ro-
 356 tated by the angle α [their nomenclature]" to overcome the unsteady transition when
 357 approaching the Ekman layer from below. Such rotation of the wind vector is *a*
 358 *posteriori* justified by the observational data that the model outcomes are com-
 359 pared to. This need for a connection of the two reference frames is a manifestation
 360 of a mismatch in the theoretical treatment of the inner and outer layer in this
 361 rotating flow configuration.

362 The text-book solution for Ekman flow makes use of the physical boundary
 363 conditions (BCs) for the ABL (no-slip at the bottom and geostrophic wind in the
 364 free atmosphere) and a constant eddy viscosity. Specifying the boundary conditions

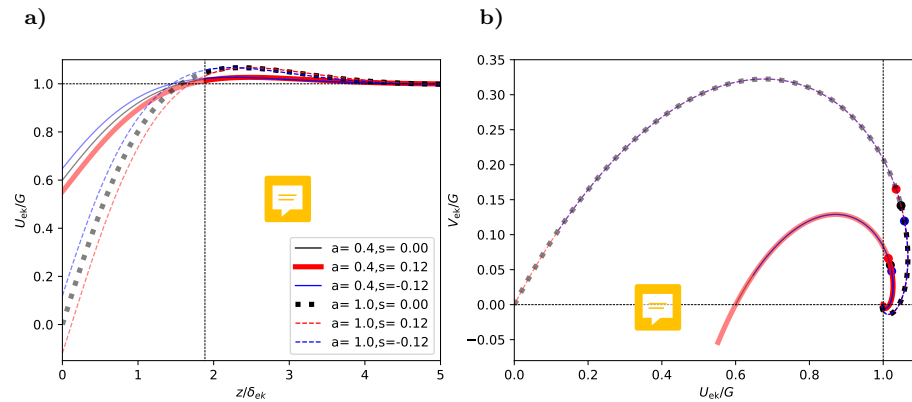


Fig. 5 a) Generalized Ekman-profile of the geostrophic-aligned component U_{ek} . b) Hodograph for the geostrophic-aligned and pressure-gradient aligned components U_{ek} and V_{ek} . Thick, black dashed line shows the classic solution. The height corresponding to $z^- = 0.30$ is marked by the dashed line in panel (a) and by filled circles in panel (b). The hodograph and profiles above this reference height are shown as solid lines, below as opaque line.

365 at top and bottom eliminates one mode of the analytical solution, and it determines
 366 the magnitude of the spiral. In doing so, one has to assume that the solution
 367 is appropriate across the entire ABL, which is not the case: The dynamics put
 368 forth by Ekman in 1905 are not appropriate in the surface layer of the ABL;
 369 better approximations exist for the logarithmic, buffer, and viscous sublayers. In
 370 view of this situation, we use an adapted Ekman spiral that does not enforce the
 371 boundary conditions at the surface but at a different height. This is achieved by
 372 considering the Ekman spiral only in the Ekman layer, thus giving way for the
 373 well-established logarithmic and viscous-layer profiles in the lower surface layer.
 374 Based on the derivation in App. A, this profile is given by

$$\frac{1}{G} \begin{pmatrix} U_{\text{ek}} \\ V_{\text{ek}} \end{pmatrix} = \begin{pmatrix} 1 \\ 0 \end{pmatrix} + e^{-z_{\text{ek}}} \left[a_{\text{ek}} \begin{pmatrix} -\cos z_{\text{ek}} \\ \sin z_{\text{ek}} \end{pmatrix} + b_{\text{ek}} \begin{pmatrix} \sin z_{\text{ek}} \\ \cos z_{\text{ek}} \end{pmatrix} \right]. \quad (11a)$$

375 with $z_{\text{ek}} = \delta_{\text{ek}}(y^- - s_{\text{ek}})$. The right-hand-side consists of two modes with magnitude
 376 a_{ek} and b_{ek} shifted by $\pi/2$ with respect to each other. In the classic case, the second
 377 mode governed by b_{ek} is incompatible with the surface boundary condition. While
 378 this is not the case here for the general form of the profile, the phase shifts can also
 379 be captured by the parameter s_{ek} , and we stick with to a single-modal approach,
 380 i.e., we let $b_{\text{ek}} = 0$.

381 This single-modal solution is characterized by three parameters, (i) an Ekman-
 382 layer depth scale δ_{ek} , (ii) the magnitude parameter of the spiral a_{ek} , and (iii) a
 383 zero-crossing point for the velocity s_{ek} . The effects of varying these parameters
 384 are illustrated in Fig. 5 where the classic Ekman solution is recovered by setting
 385 $a_{\text{ek}} = 1$, $s_{\text{ek}} = 0$ and $\delta_{\text{ek}} = \sqrt{2\nu}/f$. These parameters are *a priori* unknown as
 386 they need to conform to the turbulent state of the boundary layer; we use our
 387 DNS data to arrive at best estimates for them.

388 **The Ekman-layer depth scale** δ_{ek} is fundamentally defined by the eddy vis-
 389 cosity. However, we have seen in Section 3 that a characteristic value for the eddy
 390 diffusivity is not easily obtained for its strong dependence on the Reynolds number

and distance from the surface. We therefore resort to the physical manifestation of the eddy diffusivity in an Ekman layer, and use the boundary layer depth $\delta_{\text{ek}} = 0.66\delta \times 2\pi$. For the relation $\delta_{\text{ek}} = \sqrt{2\nu_{\text{ek}}/f}$, this yields $\nu_{\text{ek}} \propto u_*^2/f$ in accordance with the observations in Sec. 3 (Eq. 9c).

The magnitude parameter of the Ekman spiral, a_{ek} , defines the super-geostrophic maximum of the wind profile aloft the logarithmic layer. Our simulations suggest this maximum of the velocity deficit remains constant when normalized by u_* as shown in Fig. 6. The numerical value of a_{ek} is estimated from visual comparison, and we find $a_{\text{ek}} = 8.4u_*$; while this appears rather large, it is pre-multiplied by $e^{-z_{\text{ek}}}$ which has already decreased to $\mathcal{O}(0.1)$ at the height of this maximum. This choice ascertains that the velocity deficits $U/u_* - Z_*$ and $V/u_* - Z_*$ do not depend on the velocity scale u_* , but only on G as

$$U_{\text{ek}}/u_* - Z_* \propto a_{\text{ek}}Z_* = 8.4G. \quad (12)$$

Thus, the reduction of the area under the Ekman hodograph is directly linked to the variation in the friction velocity, which quantifies the well-known qualitative observation that a more turbulent boundary layer leads to a flatter hodograph in Ekman flow.

The offset parameter s_{ek} defines the zero-crossing height of the profile (in contrast to δ_{ek} , which determines the thickness across which the wind veering takes place). Physically, this offset can be understood as the height at which the surface was located assuming a perfect Ekman flow down to the surface. As this is not the case, and gradients are steeper in the highly turbulent boundary layer flow encountered when approaching the surface, the offset is smaller than zero (the fully turbulent boundary layer is actually thinner than an Ekman layer would be). From our DNS data, we estimate $s_{\text{ek}} = -0.12$.

In summary, the outer layer of Ekman flow is characterized by a turning of the wind velocity and the super-geostrophic maximum that is sustained by momentum convergence at the inflection point of the velocity profile. The super-geostrophic maximum of streamwise velocity and a secondary minimum aloft the bulk-turbulent part of the boundary layer are well-described by a classic Ekman spiral with adapted boundary conditions and a shift in reference height. Corresponding profiles are shown in comparison with data from three DNS runs in Fig. 6. The idealized profiles capture the secondary minimum and convergence to the geostrophic equilibrium in the non-turbulent flow very well.

4.3 Streamwise Velocity Component

For the streamwise velocity profile (that in non-rotating flows due to the geometry is always aligned with the surface shear stress), well-established theories exist for various regimes according to their distance from the wall and the relative role of viscosity, turbulence and interaction with the outer region of the flow with the logarithmic law for the mean velocity as a central anchor point.

In immediate vicinity to the surface, local turbulent mixing cannot occur for the no-slip/no-penetration boundary condition, and the mean velocity is described by a viscous profile of the form

$$U^{\alpha_*+} = z^+ \quad (13a)$$

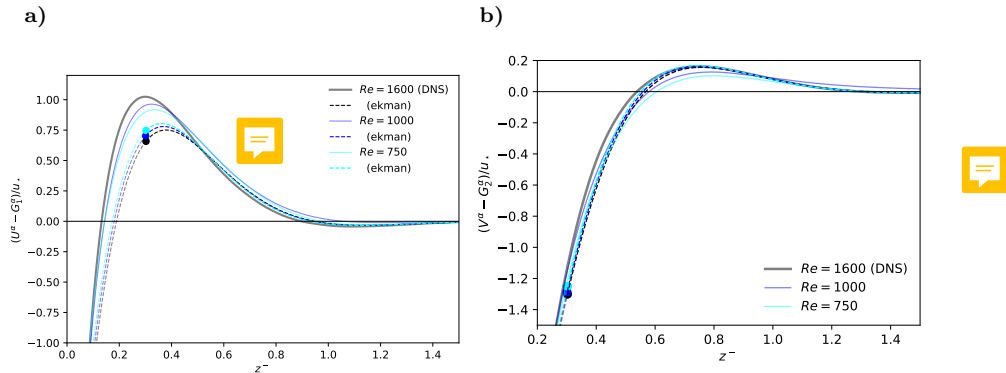


Fig. 6 Shear-aligned velocity deficit for the wall-streamwise (panel (a)) and wall-spanwise (panel (b)) components of the mean velocity U^α and V^α . Solid lines show DNS data, dashed lines the Ekman profiles U_{ek} and V_{ek} as defined in Eq. 11. Region below $z^- = 0.3$ is shown opaque. Variations in U_{ek} and V_{ek} are a consequence of the normalization and related to changes in u_* and α_* among the different Re_D .

where the direction of the velocity points into the exact opposite direction of the wall shear stress τ . In absence of roughness elements and for small roughness ($z_0^+ < 5$), this linear regime is known as viscous sub-layer Foken (2002); Foken et al. (1978). In fact, this law of the wall has no degree of freedom given the drag, i.e. once u_* and α_* are defined. However, theoretical foundation is lacking for the exact shape of the velocity profile in the buffer layer; though crucial for turbulence production, it is commonly understood as a transition region between the linear profile at the surface and the logarithmic profile aloft. A pure blending from the linear velocity profile into the logarithmic one is, however, not reasonable as both the linear and logarithmic profile overestimate the velocity in the buffer layer. We therefore introduce a two-step correction procedure, accounting for the smaller-than linear growth beyond $y^+ \approx 5$, and assuring smooth matching with the logarithmic law at $y^+ = 40$:

$$U_{\text{inner}}^{\alpha_*+} = \frac{z^+}{1 + c_1(y^+)^2} + (c_2y^+ - a_{\text{match}}) \frac{1 + \tanh[0.2(y^+ - 22)]}{2} + c_3 e^{-c_4(y^+ - 22)^2}. \quad (13b)$$

We use here

$$c_1 = 0.00185; \quad c_2 = 0.195; \quad c_3 = 0.4; \quad c_4 = 0.35.$$

The second and third terms on the right hand side vanish for $y^+ \ll 22$, and $c_1 = 0.00185$ implies an approximately 5% correction at $y^+ = 5$ and an 18.5% correction at $y^+ = 10$. The second and third term on the R.H.S. of eq. (13b) are an empirical fit to the velocity profiles observed in the buffer layer and appear independent of the Reynolds number for the range observed here. The coefficient a_{match} , which has no effect in the viscous sublayer, is then used to match this formulation to the logarithmic law employed above.

In the logarithmic region, we use the profile

$$U_{\log}^{\alpha_*+} = \frac{1}{\kappa} \log y^+ + C \quad (13c)$$

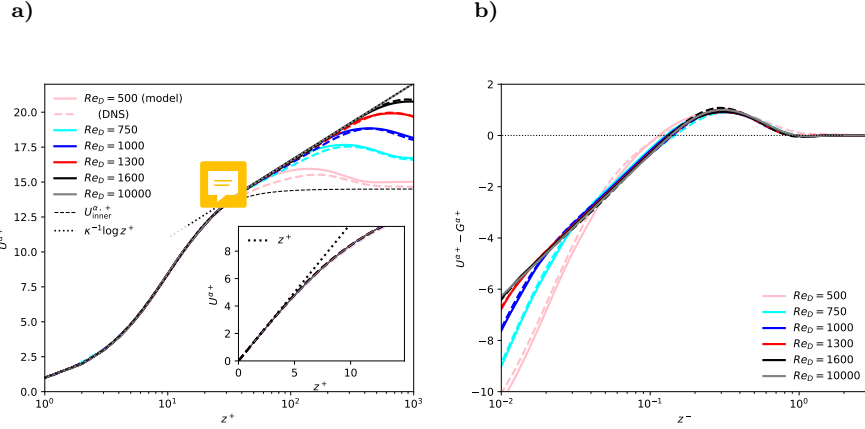


Fig. 7 Shear-aligned profiles of velocity components $U^{\alpha*+}$ in inner (left) and outer (right) units.

455 with the von-Kármán constant $\kappa = 0.416$ and the boundary condition $C = 5.4605$.
456 For this logarithmic law, $a_{\text{match}} = 3.569861$ for a matching at $y^+ = 40$.

457 4.4 Spanwise velocity component

458 The background rotation and associated veering of the surface wind implies a
459 non-zero profile for the span-wise velocity which challenges the conventional as-
460 sumptions related to the channel-flow analogy: While the analogy with channel
461 flow in vicinity of the wall implies that the streamwise component be zero or at
462 least small, the veering requires a value of $V_{top} = U_G \sin \alpha_*$ in the free stream (and
463 thus also at the top of the boundary layer if we assume that any substantial veloc-
464 ity gradient is confined to the turbulent part of the flow). This continuous rotation
465 of the wind vector is conveniently visualized by velocity hodographs aligned with
466 the outer, geostrophic flow (cf. Fig. 5b) and normalized by the geostrophic wind.
467 The geometry of the flow and its drag imply the following for any hodograph: (i)
468 the boundary conditions at the surface, (ii) the boundary condition at the top,
469 and (iii) the inclination of the hodograph at the origin by the surface veering:

$$V^{\alpha*}(z=0) = 0, \quad (14a)$$

$$\lim_{z \rightarrow \infty} V^{\alpha*} = G \sin \alpha_* \quad (14b)$$

$$\partial_{z^+} V^{\alpha*+}|_{z=0} = 0. \quad (14c)$$

470 Outer scaling of the velocity profile further implies that the velocity deficit of
471 $(V^{\alpha*} - G^{\alpha*})/u_*$ be a universal function of the outer height z^- . In the outer region
472 of the flow (for $z^- \rightarrow 1$), $f_V(z^-)$, should govern the spanwise velocity profile, as
473 is supported by our DNS data (Fig. 1b); above $z^- \approx 0.3$, this profile is very well
474 approximated by the Ekman-turning derived above (Eq. (11); Fig. 6b). While this
475 deficit is a signature of outer rotation, it is inappropriate to extend this general
476 relation to the surface where inner scales matter: On the one hand, the variation
477 of the spanwise velocity deficit across the boundary layer (i.e. between $0 < z^- < 1$)

must match the difference implied by the drag law (u_* , α_*) and the constant value of V^{α_*} around $z^- = 0.3$. On the other hand,—provided the outer velocity deficit is Re independent—the Re-dependence of α_* and u_* implies that this difference cannot be constant as a function of Re.

We hence ask, how does the span-wise component scale when the surface is approached? Clearly, the spanwise contribution is small in comparison with the streamwise component throughout much of the layer below $z^- \approx 0.3$. However, we cannot assume $V = 0$ if a smooth matching between the inner and outer layers shall be achieved. In this context, we first realize that the velocity deficit $(V^{\alpha_*} - G^{\alpha_*})/u_*$ approaches a Re-independent constant around $C_{V0} = Z_* \sin \alpha = 6.1$ at the surface; deviations from this constant are only found for the lowest Reynolds numbers which is in accordance with the low-Re correction suggested by Spalart (1989). This constrains the wind veer, and it quantitatively shows that the decreasing wall friction manifest in an increase of Z_* exactly compensates the decrease of wind turning measured by $\sin \alpha_*$.

If the difference across the boundary layer is constant (C_{V0}) vs. Re, the averaged gradient $\partial_{z+} V^{\alpha_*+}$ of the spanwise velocity component must decrease as $1/\delta^+$ with increasing Re_τ . Hence, it should—at a fixed height—be $V^{\alpha_*} \propto (\delta^+)^{-1}$. A profile that agrees with the constraints of the profile at the surface and exploits the dependence of V^{α_*} on δ^+ is

$$V^{\alpha_*} \frac{\delta^+}{G} = f_{V,\text{visc}}(z^+) = v_{\text{ref}} (\omega_v z^+ - 1 + \exp[-\omega_v z^+]), \quad (15)$$

where v_{ref} controls the magnitude of the profile and ω_v sets the height at which the profile transitions into an approximately linear one. We find excellent agreement with the DNS data for $500 \leq Re_D \leq 1600$ below $z^+ \approx 15$ with

$$v_{\text{ref}} = 18.85; \quad \omega_v = 0.2353$$

(cf. Fig. 8b).

For the adjacent surface layer, we find a log-like transition from the quasi-linear profile inner profile around $z^+ = 10$ to a linear profile with increasing Re (Fig. 8b). We model this transition by

$$f_{V,\log}(z^+) = \frac{V_{\log}(z^+)}{G} \delta^+ = a_{\log} + b_{\log} \log z^+ + c_{\log} z^+. \quad (16)$$

This surface-layer profile matches the inner (viscous) scaling in vicinity of the surface to the outer (Ekman) scaling above $z^- = 0.3$ when constrained by the viscous profile at the bottom and the Ekman profile at the top:

$$f_{V,\log}(z^+ = 10) = \quad f_{V,\text{visc}}(z^+ = 10) =: v_{10} \simeq 27.3 \quad (17)$$

$$\frac{\partial}{\partial z^+} [f_{V,\log}]_{z^+ = 10} = \quad \frac{\partial}{\partial z^+} [f_{V,\text{visc}}]_{z^+ = 10} =: d_{10} \simeq 4.01 \quad (18)$$

$$f_{V,\log}(z^+ = 0.3\delta^+) = \quad V_{\text{ek}}^{\alpha_*}(z^- = 0.3)\delta^+ =: v_{03} \quad (19)$$

where v_{03} is determined by $V_{\text{ek}}(0.3)$ and $U_{\text{ek}}(0.3)$ and depends on Re. Given the Ekman formulation of the velocity profile introduced in Sec. 4.2, one may express v_{03} using the Ekman profile introduced in Sec. 4.2 together with the approximation for $u_*(Re)$ found in Eq. (10). While the Re-dependency of a_{\log} , b_{\log} , c_{\log} is small,

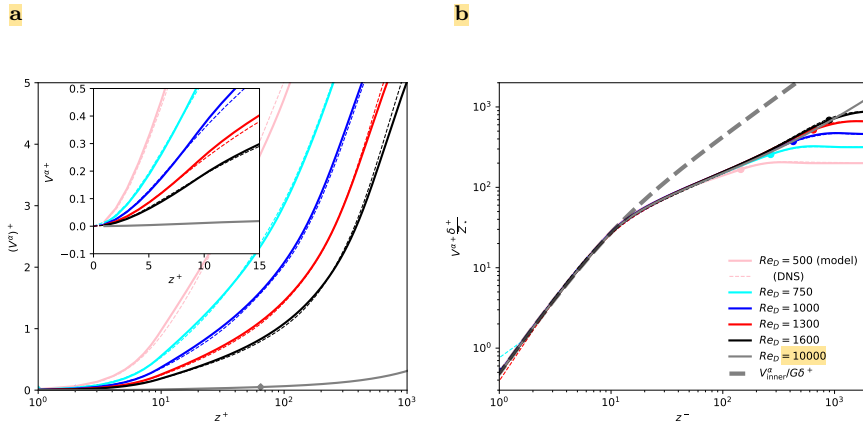


Fig. 8 Profiles of shear-aligned span-wise velocity (W^α)⁺ versus inner height. Dashed lines show DNS data, thick, opaque lines are from the semi-empirical theory developed above. **Left panel** show standard inner normalization. Right panel shows the inviscid normalization yielding a universal profile for the spanwise component of velocity in the inner layer.

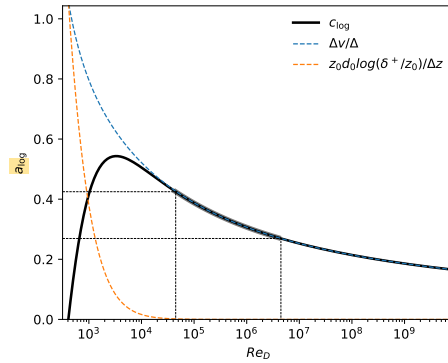


Fig. 9 Coefficients a_{\log} , b_{\log} and c_{\log} (cf. Eq. 16) as a function of the viscous Reynolds number Re_D . The approximate range of scale separation relevant for atmospheric application is found in between the dotted lines, where $a_{\log} \approx 0$ and $c_{\log} \approx 0.4$

it shows up in Fig. 1 where the normalized profiles of spanwise velocity become more convex with increasing Re . We can now quantify this effect by means of the change of c_{\log} versus Re which is shown in Fig. 9 (cf. Appendix B; a_{\log} and b_{\log} are then determined by the universal values of v_{10} and d_{10}).



5 Discussion

5.1 Implications for surface-layer scaling

Eq. (15) establishes a universal mixed scaling for the spanwise velocity in the viscous layer: While it requires the vertical coordinate to be expressed in inner units, the velocity itself is normalized by the geostrophic wind, and becomes inversely

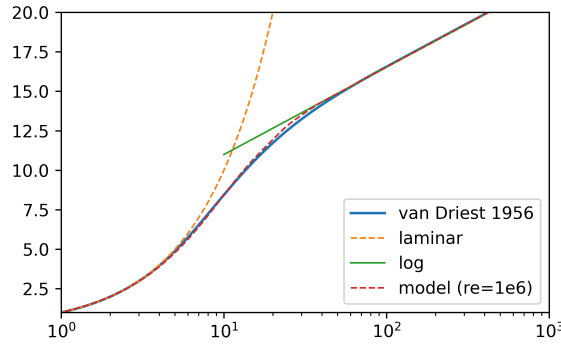


Fig. 10 Near-wall velocity profile according to the van-Driest scaling (blue, solid) in comparison with the present model (red, dashed), the viscous law of the wall (orange dashed), and the logarithmic law (green, solid)

proportional to the friction Reynolds number $\text{Re}_\tau = \delta^+$ when considered at a fixed height. In vicinity of the surface, such mixed scaling has already been identified for higher-order statistics in convective flows (Mellado et al. 2016; Li et al. 2018), where large scales leave their signatures in vicinity of the surface. It is important to note here that, while V is a first-order statistic from a statistical perspective, the spanwise velocity is a higher-order correction term from the perspective of similarity theory and from the viewpoint of the channel-flow analogy that is routinely employed in the surface layer. Further, this is consistent with the scaling for the velocity hodograph found in Eq. (12) **where the friction velocity also drops out**.

In the surface layer, there is not only a mixed scaling—as we had already identified in the viscous layer—but we cannot find a universal function onto which the profiles of spanwise velocity collapse. This additional degree of freedom reflects the inner–outer matching problem for the spanwise velocity, and rather than giving a universal profile for this region, as is usually done, we resort here to a parametric description of the problem, namely in terms of the function $f_{V,\log}$ determined by the parameters a_{\log} , b_{\log} , c_{\log} which can be estimated based on the above scaling considerations for any Reynolds number. We note that, once the parameter a_{\log} is known, the parameters b_{\log} and c_{\log} can be estimated solely based on $f_{V,\text{visc}}$, i.e. using the value v_{10} and d_{10} found for the viscous region of the flow. For the range of Reynolds number relevant to geophysical problems ($10^4 \lesssim \text{Re}_D \lesssim 10^6$), the variation of c_{\log} is, however, rather small.

5.2 Comparison with other theories

An alternative approach that considers viscous effects close to the surface is the van-Driest scaling (Van Driest 1956), where an exponential damping of Prandtl's mixing length is considered near the wall to yield

$$\frac{\partial u^+}{\partial y^+} = \frac{2}{1 + \sqrt{1 + (2\kappa y^+)^2} (1 - \exp[-y^+])}; \quad (20)$$

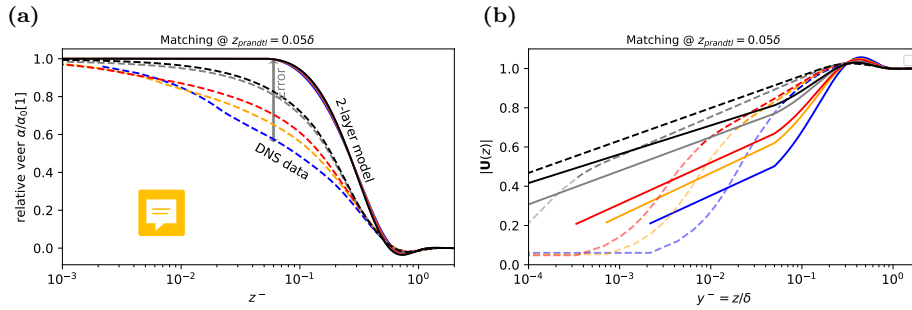


Fig. 11 Comparison of the DNS data (dashed lines) with the two-layer model proposed by Etling (solid lines) for different Reynolds number. Left panel shows the relative wind veer, right panel shows the velocity magnitude. The Etling model is calibrated by the surface veer from the DNS and roughness parameter for the Etling model is chosen according to the correction factor $\exp \kappa A$ such that the total veer and velocity magnitude agree. DNS profile in the buffer layer, defined here as $z^+ < 30$ are shown as opaque dashed lines as the two-layer model does not consider viscous effects.

the spanwise component is zero as no rotational effects are considered. Comparing our proposed formulation (Fig. 10) for the stream-wise velocity in the inner layer to Van Driest's formulation yields later convergence of the velocity onto the logarithmic profile while, over all, it serves as an excellent model of the streamwise velocity component: Notable deviations (on the order of few percent) only occur in the region $10 < z^+ < 30$, where the velocity transitions from the linear to the logarithmic profile.

For the higher layers of the ABL, the Ekman spiral is the simplest model available. When employed across the entirety of the ABL, the spiral of a turbulent Ekman layer is flattened with respect to Ekman's laminar solution, which corresponds to a reduction of the veering angle both at the surface and throughout the ABL. We, however, find that a modified version of the Ekman spiral explicitly taking into account the surface boundary condition, is a consistent model and yields excellent agreement with the velocity profiles from DNS (Sec. 4.2).

A two-layer model consolidating both the logarithmic and Ekman layer can be obtained following the arguments by Etling (2008), cf. Emeis (2018). Given a surface veering and a matching height (extent of the logarithmic layer), a formulation for the velocity profile across both the logarithmic and the outer layer is obtained. A comparison using the surface veering based on our model and a matching height of $z_{\text{prandtl}} = 0.05\delta$, which gives better results than the matching height of 0.1δ suggested by Etling (2008), is shown in Fig. 11. The overall shape of velocity magnitude is matched apart from the viscous and buffer layer (cf. Fig. 11b) that is neglected by the two-layer model. However, quantitative departures on the order of 10% occur across the inner layer: it turns out that the non-rotating profile, of the two-layer model in the logarithmic region yields too low overall velocity as the spanwise component contributes to the velocity across the inner layer. Deviations also occur with respect to wind direction; despite the rather low matching height, a substantial fraction of the rotation occurs within the lower part of the ABL and about 20% of the wind veer is not captured by the two-layer model. As the overall veer is given, the non-captured veer close to the

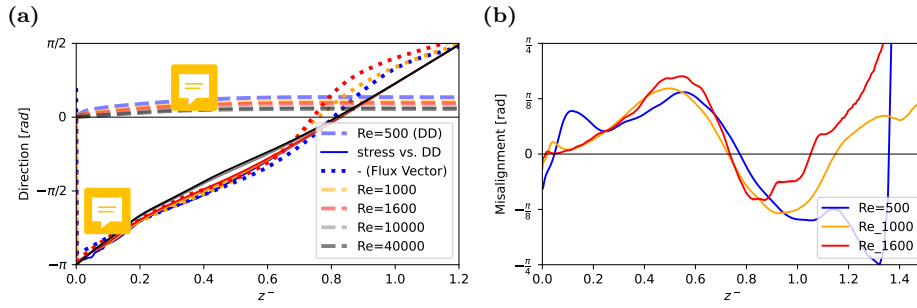


Fig. 12 Panel (a) shows the wind direction (DD) as thick dashed lines and the direction of stress relative to DD as thin solid lines, both according to our profile model. The direction of the negative flux vector ($u'w', v'w'$) based on DNS data is shown as a dotted line. In panel (b), we plot the misalignment, i.e. the angle, between the flux vector and the shear vector, where the shear vector is defined accordingly as $(\partial_z U, \partial_z V)$.

576 surface is then compensated across the logarithmic layer. In the upper part of the
577 boundary layer, both profiles match well.

578 The interpretation of flux and gradient profiles in terms of the K-theory (cf.
579 Sec. 3, Fig. 2) suggests a certain universality in the inner layer, while a global
580 collapse, i.e. across the boundary layer, is not obtained. While the K-Profiles con-
581 cern the total stress, a consistent formulation of the turning would also require its
582 partitioning to the individual components, i.e. the orientation of the stress vector
583 ($u'w', v'w'$) in the horizontal plane. If K-theory shall be used, this stress vector
584 needs to be anti-parallel to the corresponding stress vector ($\partial_z U, \partial_z V$). Fig. 12
585 shows the direction of the **velocity, gradient** and stress vectors across the bound-
586 ary layer. It turns out that the negative stress vector with respect to the wind
587 direction and the flux vectors (absolute) have an approximately similar direction.
588 It appears that both rotate by about 270° ($3\pi/2$) across the boundary layer. Apart
589 from the lower part of the Ekman layer ($0.2 < z^- < 0.7$), where there is a slight
590 dependence on Re , the direction of stress appears to be universal, which is a con-
591 sequence of the Ekman profile introduced in Sec. 4.2. However, this implies **the a**
592 misalignment between the flux and the stress on the order of the wind turning,
593 and indeed Fig. 12b shows a **misalignment up to 90°** . This is in accordance with
594 the expectation by (Townsend 1976, §7.18) and prevents the transfer of **Energy**
595 from the mean flow to turbulence at these heights, thus preventing a boundary-
596 layer growth. While the behavior in the inner layer seems to depend on Re , there
597 emerges universality in the misalignment across the outer layer, suggesting that a
598 universal consideration of misalignment in the context of K-theory is possible for
599 formulations of higher-order quantities.

600 6 Conclusions

601 We investigate the wind veer in Ekman flow. Based on scaling considerations
602 and direct numerical simulation spanning **on** decade in external separation from
603 $Re_A = 1.25 \times 10^5$ to $Re_A = 1.28 \times 10^6$, we derive a universal formulation for the
604 both horizontal components of the velocity profile in a stationary, smooth Ekman
605 layer. This formulation is consistent with the DNS data and also yields reasonable

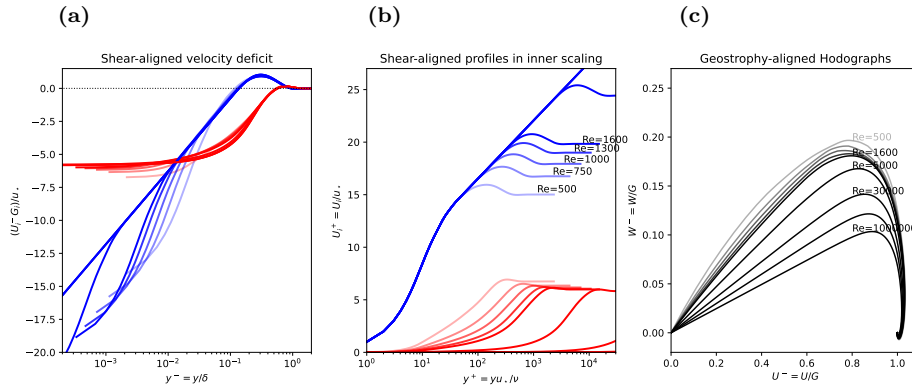


Fig. 13 (a) Velocity deficit, (b) velocity profile in shear-aligned hodographs and (c) hodograph in geostrophy-aligned coordinates. Thick, solid lines show theory, dashed lines data from DNS.

606 results at geophysical scale separation; the logarithmic law of the mean velocity
 607 is recovered with the well-known limits and deviations towards the surface and
 608 Ekman layer. The classic formulation of the Ekman layer, employing the surface
 609 boundary condition, is replaced by a modified solution that can be obtained by
 610 Ekman's system of governing equations, but using different boundary conditions
 611 that are more appropriate of the actual situation encountered in the planetary
 612 boundary layer. The three parameters that characterize this boundary condition
 613 are estimated based on DNS data.

614 To quantify the spanwise velocity component consistently across the boundary
 615 layer, we derive a universal scaling of the spanwise velocity component in a shear-
 616 aligned reference frame. For the *inner layer*, we find the mixed scaling

$$V^{\alpha_*}/G = \frac{1}{\delta^+} f(z^+),$$

617 that is, the spanwise velocity normalized by the outer velocity scale is a universal
 618 function of the inner height and Friction Reynolds number $Re_\tau = \delta^+$. This scaling
 619 is derived here based on scaling considerations, and it is in excellent agreement
 620 with the DNS data available. In the outer layer, the spanwise velocity follows outer
 621 scaling, consistently with the Ekman model mentioned above (Sec. 4.2).

622 The velocity profiles are shown in inner and outer scaling as well as in ho-
 623 dograph-view in Fig. 13. The shear-aligned velocity deficit is shown in outer
 624 scaling highlighting the universality in the outer layer. In the inner layer, the
 625 logarithmic profile (blue, panel (b)) is encountered across a widening region for
 626 increasing Reynolds number. In this simple inner scaling, the spanwise velocity scales
 627 (which follows a mixed scaling) does not collapse but seems to depend on Re (the
 628 collapse is seen in Fig. 8). While, at a fixed height, the spanwise velocity scales
 629 approximately as Re_τ^{-1} , the fraction of turning that is encountered within the
 630 inner layer of the flow amounts to about 1/3 of the total wind veer (Fig. 11a).
 631 The hodographs show the well-known Ekman shape with the laminar profile as an
 632 outer limit and 'flatter' hodographs, corresponding to less turning, for increasing
 633 Reynolds number. Importantly, our results suggest that there is no lower limit of
 634 the turning. This implies that, despite its very large scale separation and huge

635 Reynolds number, the ABL cannot be in the 'limit' of high Reynolds number from
 636 the perspective of wind veer.



637 Laminar Ekman solution with consideration of inner layer

$$\begin{pmatrix} \partial_t U \\ \partial_t W \end{pmatrix} = \begin{pmatrix} fW \\ -f(U - G) + \nu \partial_z^2 W \end{pmatrix} \quad (21a)$$

$$\Rightarrow \partial_t(U + iW) = f(W - i(U - G)) + \nu \partial_z^2(U + iW) \quad (21b)$$



638 In stationary conditions, this system is solved by

$$\hat{u}(z) = U_\infty + e^{-\gamma z} [A \cos \gamma z + B \sin \gamma z] \quad (21c)$$

$$\hat{w}(z) = W_\infty + e^{-\gamma z} [-A \sin \gamma z + B \cos \gamma z] \quad (21d)$$

639 where the constants U_∞ , W_∞ set the top boundary condition and A and B set the bottom
 640 boundary condition. The most common boundary condition for a surface Ekman layer is $A =$
 641 $U_\infty = G$, $B = 0$, and $W_\infty = 0$. The lower boundary condition, however, neglects the existence
 642 of the surface layer, and it appears reasonable to define $A = cG$ where $c < 1$ is a constant
 643 that incorporates the increased shear in the surface layer. Given a 'matching height' z_{match} and
 644 normalized matching height $\xi = \gamma z_{match}$ in the upper part of the inner layer, we can match
 645 the Ekman profile to the inner layer by letting

$$\begin{aligned} u(z_{match}) &\equiv u_{match} = U_\infty + e^{-\xi} [A \cos \xi + B \sin \xi] \\ w(z_{match}) &\equiv w_{match} = W_\infty + e^{-\xi} [-A \sin \xi + B \cos \xi] \end{aligned} \quad (22)$$

646

$$\Rightarrow \begin{pmatrix} u_{match} - U_\infty \\ w_{match} - W_\infty \end{pmatrix} = e^{-\xi} \begin{pmatrix} A \\ B \end{pmatrix} \begin{pmatrix} \cos \xi & +\sin \xi \\ -\sin \xi & +\cos \xi \end{pmatrix} \quad (23)$$

$$(24)$$

647 Matching the profile at $\xi = 0$, one obtains $A = \Delta u_{match}$ and $B = -\Delta w_{match}$; and when the
 648 direction Ox is aligned with the geostrophic wind, we obtain the textbook-case $A = |\mathbf{G}|$ and
 649 $B = 0$.

650 Otherwise, choosing $B \neq 0$ allows to introduce a phase shift of the Ekman rotation with
 651 respect to the decay of the wind spiral. As, however, in our context, the thickness and position
 652 of the spiral can already be controlled by the eddy viscosity and an offset in ζ , here we let
 653 $B = 0$.

654 **B Matching the spanwise velocity profiles in the inner layer**

655 The spanwise profile in vicinity of the surface is given by $V/G = f_{V,visc} \delta^+$ with

$$f_{V,visc} = v_{ref} (\omega_v z^+ - 1 + e^{-\omega_v z^+}) \quad (25a)$$

$$f_{V,log} = a_{log} + b_{log} \log z^+ + c_{log} z^+ \quad (25b)$$

656 Matching the profiles and gradient $z_0 = 10^+$ and the value at $z_1 = 0.3\delta^+$ yields

$$v_{ref} (\omega_v z_0 + e^{-\omega_v z_0}) = v_0 = a_{log} + b_{log} \log z_0 + c_{log} z_0 \quad (26a)$$

$$v_1 = a_{log} + b_{log} \log z_1 + c_{log} z_1 \quad (26b)$$

$$v_{ref} \omega_z (1 - e^{-\omega_z z_0}) = d_0 = \frac{b_{log}}{z_{10}} + c_{log} \quad (26c)$$

657 The gradient condition implies $b_{\log} = (d_0 - c_{\log})z_0$, and yields

$$v_0 - z_0 d_0 \log z_0 = a_{\log} + c_{\log}(z_0 - z_0 \log z_0) \quad (27a)$$

$$v_1 - z_0 d_0 \log z_1 = a_{\log} + c_{\log}(z_1 - z_0 \log z_0) \quad (27b)$$

$$\Rightarrow c_{\log} = \frac{\Delta v - z_0 d_0 \log z_1 / z_0}{\Delta z} \quad (27c)$$

658 with $\Delta z = z_1 - z_0$ and $\Delta v = v_1 - v_0$. Then, the coefficient a_{\log} is estimated as

$$a_{\log} = v_0 - z_0 d_0 \log z_0 - \frac{\Delta v - z_0 d_0 \log z_1 / z_0}{\Delta z} [z_0 - z_0 \log z_0]. \quad (27d)$$

659 We note that $\log(z_1/z_0)/(z_1 - z_0) \rightarrow 0$ for large z_1 , and as $z_1 = 0.38^+$, this implies that the
660 second term in c_{\log} only plays a role at low and intermediate Re. Then, a_{\log} can be estimated
661 as

$$a_{\log} \simeq v_0 - z_0 \left[d_0 \log z_0 - \frac{\Delta v}{\Delta z} (1 - \log z_0) \right] \quad (27e)$$

662 for large Re.

663 **Acknowledgements** This study is funded by the European Commission's 7th Framework Pro-
664 gramme through the ERC 2019 Starting Grant *trainABL* (ID 851374). Simulations were carried
665 out on the German supercomputing systems **hawk** at Höchstleistungsrechenzentrum Stuttgart
666 (Bundesprojekt 44187) and **juwels** at Gauss Centre for supercomputing, Forschungszentrum
667 Jülich (Projects **hku24** and **stadit**). We extend our thanks to Sally Issa for valuable feedback
668 on the manuscript.

669 Declarations

670 **Author Contributions** CA conceived the study, acquired funding, performed the simulation,
671 analysed and plotted the data for this work. CA and HW interpreted the data and compiled
672 the manuscript.

673 **Funding** CA is funded by ERC Starting Grant *trainABL* (ID 851374). Open Access funding
674 for this publication through the DEAL agreement.

675 **Data Availability** The data is available in long-term repositories and indexed by DOIs as
676 cited in the list of references. Further analysis tools and processed data can be made available
677 upon direct request.

678 **Conflict of Interest** The Authors declare no competing interest.

679 **Open Access** This article is licensed under a Creative Commons Attribution 4.0 International
680 License, which permits use, sharing, adaptation, distribution and reproduction in any medium
681 or format, as long as you give appropriate credit to the original author(s) and the source,
682 provide a link to the Creative Commons licence, and indicate if changes were made. To view
683 a copy of this licence, visit <https://creativecommons.org/licenses/by/4.0/>.

684 References

- 685 Ansorge C (2019) Scale Dependence of Atmosphere–Surface Coupling Through Similarity The-
686 ory. *Boundary-Layer Meteorol* 170(1):1–27, DOI 10.1007/s10546-018-0386-y
687 Ansorge C (2024a) Direct numerical simulation of turbulent Ekman flow (Re=0500): DOI
688 10.17169/refubium-42505. DOI 10.17169/refubium-42505
689 Ansorge C (2024b) Direct numerical simulation of turbulent Ekman flow (Re=1000): DOI
690 10.17169/refubium-42507. DOI 10.17169/refubium-42507

- Ansorge C (2024c) Direct numerical simulation of turbulent Ekman flow ($Re=1300$): DOI 10.17169/refubium-42508. DOI 10.17169/refubium-42508
- Ansorge C (2024d) Direct numerical simulation of turbulent Ekman flow ($Re=1600$): DOI 10.17169/refubium-42509. DOI 10.17169/refubium-42509
- Ansorge C, Mellado JP (2014) Global Intermittency and Collapsing Turbulence in the Stratified Planetary Boundary Layer. *Boundary-Layer Meteorol* 153(1):89–116, DOI 10.1007/s10546-014-9941-3
- Ansorge C, Mellado JP (2016) Analyses of external and global intermittency in the logarithmic layer of Ekman flow. *J Fluid Mech* 805:611–635, DOI 10.1017/jfm.2016.534
- Baars WJ, Marusic I (2020) Data-driven decomposition of the streamwise turbulence kinetic energy in boundary layers. Part 2. Integrated energy and. *J Fluid Mech* 882:A26, DOI 10.1017/jfm.2019.835
- Barenblatt GI (1993) Scaling laws for fully developed turbulent shear flows. Part 1. Basic hypotheses and analysis. *J Fluid Mech* 248:513–520, DOI 10.1017/S0022112093000874
- Barenblatt GI, Goldenfeld N (1995) Does fully developed turbulence exist? Reynolds number independence versus asymptotic covariance. *Phys Fluids* 7(12):3078–3082, DOI 10/bw2sq8
- Blackadar AK, Tennekes H (1968) Asymptotic Similarity in Neutral Barotropic Planetary Boundary Layers. *Journal of the Atmospheric Sciences* 25:1015–1020, DOI 10.1175/1520-0469(1968)025<1015:ASINBP>2.0.CO;2
- Brown AR, Beljaars ACM, Hersbach H, Hollingsworth A, Miller M, Vasiljevic D (2005) Wind turning across the marine atmospheric boundary layer. *Quarterly Journal of the Royal Meteorological Society* 131(607):1233–1250, DOI 10/dw2bxz
- Calaf M, Meneveau C, Meyers J (2010) Large eddy simulation study of fully developed wind-turbine array boundary layers. *Phys Fluids* 22(1):015,110, DOI 10/b7gc6v
- Coleman GN, Ferziger JH, Spalart PR (1992) Direct Simulation of the Stably Stratified Turbulent Ekman Layer. *Journal of Fluid Mechanics* 244:677–712, DOI 10.1017/S0022112092003264
- da Silva CB, Hunt JC, Eames I, Westerweel J (2014) Interfacial Layers Between Regions of Different Turbulence Intensity. *Annu Rev Fluid Mech* 46(1):567–590, DOI 10.1146/annurev-fluid-010313-141357
- Dimotakis PE (2005) TURBULENT MIXING. *Annual Review of Fluid Mechanics* 37(1):329–356, DOI 10.1146/annurev.fluid.36.050802.122015
- Ekman VW (1905) On the influence of the earth's rotation on ocean currents. *Ark Mat Astron Fys, Vol 2* (1905), pp 1-53 2:1–53
- Ellison TH (1955) The Ekman spiral. *Q J Roy Met Soc* 81(350):637–638, DOI 10.1002/qj.49708135025
- Emeis S (2018) Wind Energy Meteorology, 2nd edn. *Atmospheric Physics for Wind Power Generation*, Springer, Heidelberg
- Emeis S, Baumann-Stanzer K, Piringer M, Kallistratova M, Kouznetsov R, Yushkov V (2007) Wind and turbulence in the urban boundary layer analysis from acoustic remote sensing data and fit to analytical relations. *metz* 16(4):393–406, DOI 10.1127/0941-2948/2007/0217
- Esau I (2004) Simulation of Ekman Boundary Layers by Large Eddy Model with Dynamic Mixed Subfilter Closure. *Environmental Fluid Mechanics* 4(3):273–303, DOI 10/b8f3kh
- Etling D (2002) *Theoretische Meteorologie*, 2nd edn. Eine Einführung, Springer-Verlag, Berlin, Heidelberg
- Etling D (2008) *Theoretische Meteorologie: eine Einführung*, 3rd edn. Springer, Berlin Heidelberg
- Foken T (2002) Some aspects of the viscous sublayer. *metz* 11(4):267–272, DOI 10.1127/0941-2948/2002/0011-0267
- Foken Th, Kitajgorodskij SA, Kuznecov OA (1978) On the dynamics of the molecular temperature boundary layer above the sea. *Boundary-Layer Meteorol* 15(3):289–300, DOI 10.1007/BF02652602
- Ghannam K, Bou-Zeid E (2021) Baroclinicity and directional shear explain departures from the logarithmic wind profile. *Quarterly Journal of the Royal Meteorological Society* 147:434–464, DOI 10/gnj6z2
- Gryning SE, Batchvarova E, Brümmer B, Jørgensen H, Larsen S (2007) On the extension of the wind profile over homogeneous terrain beyond the surface boundary layer. *Boundary-Layer Meteorol* 124(2):251–268, DOI 10.1007/s10546-007-9166-9
- Högström U (1988) Non-dimensional wind and temperature profiles in the atmospheric surface layer: A re-evaluation. *Boundary-Layer Meteorology* 42:55–78, DOI 10.1007/BF00119875

- 751 Höglström U (1996) Review of some basic characteristics of the atmospheric surface layer.
752 Boundary-Layer Meteorology 78(3-4):215–246, DOI 10.1007/BF00120937
- 753 Jacobs AF, Van Boxel JH (1988) Changes of the displacement height and roughness length
754 of maize during a growing season. Agricultural Forest Meteorol 42(1):53–62, DOI 10.1016/
755 0168-1923(88)90066-4
- 756 Jiang Q, Wang S, Sullivan P (2018) Large-Eddy Simulation Study of Log Laws in a Neutral
757 Ekman Boundary Layer. Journal of the Atmospheric Sciences 75(6):1873–1889, DOI 10.
758 1175/JAS-D-17-0153.1
- 759 Jiménez J (2012) Cascades in Wall-Bounded Turbulence. Ann Rev Fluid Mech 44(Volume 44,
760 2012):27–45, DOI 10.1146/annurev-fluid-120710-101039
- 761 Kelly M, Gryning SE (2010) Long-Term Mean Wind Profiles Based on Similarity Theory.
762 Boundary-Layer Meteorol 136(3):377–390, DOI 10.1007/s10546-010-9509-9
- 763 Kelly M, Troen I (2016) Probabilistic stability and ‘tall’ wind profiles: Theory and method for
764 use in wind resource assessment. Wind Energy 19(2):227–241, DOI 10.1002/we.1829
- 765 Klein M, Maier RE, Schmidt H (2021) Stochastic modeling of transient neutral and stably-
766 stratified Ekman boundary layers. P A M M 21(1):e202100146, DOI 10.1002/pamm.
767 202100146
- 768 Li Q, Gentine P, Mellado JP, McColl KA (2018) Implications of Nonlocal Transport and
769 Conditionally Averaged Statistics on Monin–Obukhov Similarity Theory and Townsend’s
770 Attached Eddy Hypothesis. J Atmos Sci 75(10):3403–3431, DOI 10.1175/JAS-D-17-0301.1
- 771 Lindvall J, Svensson G (2019) Wind turning in the atmospheric boundary layer over land. Q
772 J Roy Met Soc 145(724):3074–3088, DOI 10.1002/qj.3605
- 773 Mellado J, Ansorge C (2012) Factorization of the Fourier transform of the pressure-Poisson
774 equation using finite differences in colocated grids. Z angew Math Mech 92(5):380–392,
775 DOI 10.1002/zamm.201100078
- 776 Mellado JP, van Heerwaarden CC, Garcia JR (2016) Near-Surface Effects of Free Atmosphere
777 Stratification in Free Convection. Boundary-Layer Meteorol 159(1):69–95, DOI 10.1007/
778 s10546-015-0105-x
- 779 Mirocha JD, Churchfield MJ, Muñoz-Esparza D, Rai RK, Feng Y, Kosović B, Haupt SE,
780 Brown B, Ennis BL, Draxl C, Sanz Rodrigo J, Shaw WJ, Berg LK, Moriarty PJ, Linn RR,
781 Kotamarthi VR, Balakrishnan R, Cline JW, Robinson MC, Ananthan S (2018) Large-eddy
782 simulation sensitivities to variations of configuration and forcing parameters in canonical
783 boundary-layer flows for wind energy applications. Wind Energy Science 3(2):589–613, DOI
784 10/gn3nh4
- 785 Moin P, Mahesh K (1998) Direct numerical simulation: A tool in turbulence research. Annual
786 Review of Fluid Mechanics 30:539–578, DOI 10.1146/annurev.fluid.30.1.539
- 787 Momen M, Bou-Zeid E (2016) Large-Eddy Simulations and Damped-Oscillator Models of the
788 Unsteady Ekman Boundary Layer*. Journal of the Atmospheric Sciences 73(1):25–40, DOI
789 10.1175/JAS-D-15-0038.1
- 790 Momen M, Bou-Zeid E, Parlange MB, Giometto M (2018) Modulation of Mean Wind and
791 Turbulence in the Atmospheric Boundary Layer by Baroclinicity. Journal of the Atmospheric
792 Sciences 75(11):3797–3821, DOI 10/gfmn67
- 793 Monin AS (1970) The Atmospheric Boundary Layer. Annual Review of Fluid Mechanics 2:225–
794 250, DOI 10.1146/annurev.fl.02.010170.001301
- 795 Monin AS, Yaglom AM (1975) Statistical Fluid Mechanics, Vol. II, Dover Publications on
796 Physics, vol II. Dover Publications, Inc., Mineola
- 797 Optis M, Monahan A, Bosveld FC (2014) Moving Beyond Monin-Obukhov Similarity The-
798 ory in Modelling Wind-Speed Profiles in the Lower Atmospheric Boundary Layer un-
799 der Stable Stratification. Boundary-Layer Meteorology 153(3):497–514, DOI 10.1007/
800 s10546-014-9953-z
- 801 Rossby CG, Montgomery RB (1935) The layer of frictional influence in wind and ocean cur-
802 rents. Papers in Physical Oceanography and Meteorology III(3):1–101
- 803 Sakagami Y, Haas R, Passos JC (2020) Generalized Non-dimensional Wind and Temperature
804 Gradients in the Surface Layer. Boundary-Layer Meteorol 175(3):441–451, DOI 10.1007/
805 s10546-020-00510-3
- 806 Spalart PR (1989) Theoretical and numerical study of a three-dimensional turbulent boundary
807 layer. J Fluid Mech 205(-1):319, DOI 10.1017/S0022112089002053
- 808 Spalart PR, Coleman GN, Johnstone R (2008) Direct numerical simulation of the Ekman layer:
809 A step in Reynolds number, and cautious support for a log law with a shifted origin. Phys
810 Fluids 20(10):101,507, DOI 10.1063/1.3005858

- 811 Spalart PR, Coleman GN, Johnstone R (2009) Retraction: “Direct numerical simulation of the
812 Ekman layer: A step in Reynolds number, and cautious support for a log law with a shifted
813 origin” [Phys. Fluids 20, 101507 (2008)]. Phys Fluids 21(10):109,901, DOI 10.1063/1.3247176
814 Stoll R, Gibbs JA, Salesky ST, Anderson W, Calaf M (2020) Large-Eddy Simulation of the At-
815mospheric Boundary Layer. Boundary-Layer Meteorol 177(2-3):541–581, DOI 10/gmbmzw
816 Svensson G, Holtslag AAM (2009) Analysis of Model Results for the Turning of the Wind
817 and Related Momentum Fluxes in the Stable Boundary Layer. Boundary-Layer Meteorol
818 132(2):261–277, DOI 10/bwknmt
819 Tennekes H (1973) A Model for the Dynamics of the Inversion Above a Convective Boundary
820 Layer. Journal of the Atmospheric Sciences
821 Townsend AA (1976) The Structure of Turbulent Shear Flow, 2nd edn. Cambridge University
822 Press
823 Van Driest ER (1956) On Turbulent Flow Near a Wall. Journal of the Aeronautical Sciences
824 23(11):1007–1011, DOI 10.2514/8.3713
825 Zikanov O, Slinn DN, Dhanak MR (2003) Large-eddy simulations of the wind-induced turbu-
826 lent Ekman layer. J Fluid Mech 495:343–368, DOI 10/ccbpbw